



Originally published as:

Hassanzadegan, A., Guerizec, R., Reinsch, T., Blöcher, G., Zimmermann, G., Milsch, H. (2016): Static and Dynamic Moduli of Malm Carbonate: A Poroelastic Correlation. - *Pure and Applied Geophysics*, 173, 8, pp. 2841–2855.

DOI: <http://doi.org/10.1007/s00024-016-1327-7>

Static and dynamic moduli of Malm carbonate: a poroelastic correlation

A. Hassanzadegan R. Guérizec T. Reinsch
G. Blöcher G. Zimmermann H. Milsch

Received: date / Accepted: date

Abstract

The static and poroelastic moduli of a porous rock, e.g. the drained bulk modulus, can be derived from stress-strain curves in rock mechanical tests and the dynamic moduli, e.g. dynamic Poisson's ratio, can be determined by acoustic velocity and bulk density measurements. As static and dynamic elastic moduli are different a correlation is often required to populate geomechanical models. A novel poroelastic approach is introduced to correlate static and dynamic bulk moduli of outcrop analogues samples, representative of Upper-Malm reservoir rock in the Molasse basin, southwestern Germany. Drained andunjacketed poroelastic experiments were performed at two different temperature levels (30 and 60 °C). For correlating the static and dynamic elastic moduli, a drained acoustic velocity ratio is introduced, corresponding to the drained Poisson's ratio in poroelasticity. The strength of poroelastic coupling, i.e. the product of Biot and Skempton coefficients here, was the key parameter. The value of this parameter decreased with increasing effective pressure by about 56% from 0.51 at 3 MPa to 0.22 at 73 MPa. In contrast, the maximum change in P- and S-wave velocities was only 3% in this pressure range. This correlation approach can be used in characterizing underground reservoirs, and can be employed to relate seismicity and geomechanics (seismo-mechanics).

1 Introduction

The static elastic moduli of a porous rock can be derived from stress-strain curves in rock mechanical tests and the dynamic moduli can be determined by acoustic velocity measurements. Static and dynamic elastic properties of porous media and their pressure and temperature dependence are of interest in many research areas, including materials science, design of foundations, mine openings, geophysical exploration, reservoir geomechanics, etc.

Injection and production of water in geothermal reservoirs leads to changes in reservoir pore pressure, resulting in changes in the stress acting on the reservoir and the surrounding rocks. A decrease in pore pressure due to production

causes an increase in stress carried by the rock skeleton and may be accompanied by microscale deformation mechanisms such as cement breakage, grain sliding, Hertzian cracking at grain contact points, plastic deformation of Clay, and opening and closure of microcracks (Sayers and Schutjens, 2007).

The static elastic moduli are representative of stress and strain changes within the reservoir, since the dynamic measurements mainly capture the elastic response of the rock (Yale and Jamieson, 1994). Therefore, it is required to convert the dynamic moduli to their equivalent static moduli. The quantitative correlation between static and dynamic moduli in combination with sonic logs and seismic data provide the input elastic parameters to populate geomechanical models. Such geomechanical models can be employed to predict the induced stresses and the resulting deformation, caused by production and injection of water from and into geothermal reservoirs, respectively (Cacace et al, 2013; Hofmann et al, 2014).

Previous studies indicated that static and dynamic moduli are often not equal, the dynamic modulus is generally larger than the static one (Simmons and Brace, 1965; King, 1969). Furthermore, the degree and range of nonlinearity of elastic moduli as a function of effective pressure are different for static and dynamic elastic moduli. Empirical relationships were often employed to relate static and dynamic moduli. Wang (2000) reviewed the empirical relationships between dynamic and static data of dry rocks. Wang (2000) obtained different correlations, depending on whether the Young’s modulus E is lower or higher than 15 GPa. Simmons and Brace (1965) measured the compressibility of some types of rocks by employing both static and dynamic approach. They found that at pressures higher than 200 MPa, the static and dynamic bulk moduli are almost equal. Heerden (1987) and Eissa and Kazi (1988) suggested a power law correlation between static and dynamic Young’s moduli. A more recent approach by Fjaer (1999) and Holt et al (2012) introduced an inelastic strain parameter and obtained the following empirical relationship between static and dynamic moduli:

$$K_d = \frac{K_u^{dy}}{1 + \frac{3K_u^{dy}}{a+b\sigma_{kk}}} \quad (1)$$

where K_u^{dy} is the dynamic undrained bulk modulus and K_d is the static drained bulk modulus, a and b are fitting parameters, and σ_{kk} is the hydrostatic stress (i.e. the first stress invariant).

This experimental study investigates the static and dynamic elastic moduli of outcrop rock samples, considered as analogous of Upper-Malm reservoirs. Accordingly, the isothermal static and dynamic moduli were measured under drained and unjacketed conditions at two temperature levels (30 and 60 °C). A novel method was developed to correlate the static and dynamic moduli, which can later be used to populate geomechanical models, to monitor the reservoir behavior using 4D seismic data, and for characterizing low effective pressure zones after earthquakes (Segall, 1989; Brenguier et al, 2014). In other words, this correlation approach can be used in relating seismicity and geomechanics

(seismo-mechanics). Moreover, the results are useful to describe the poroelastic behavior of Malm carbonate.

2 Quasi-static and dynamic theories of poroelasticity

Biot's theory of poroelasticity (Biot, 1941) and the Gassmann equation (Gassmann, 1951) are the key elements in elasticity analysis of fluid saturated porous rock (see Appendix A). The constitutive models in quasi-static poroelasticity can either be described by Biot theory (energy consideration) or by micromechanics (Nur and Byerlee, 1971; Carroll, 1980). Biot theory of poroelasticity was reviewed in an earlier study by the authors (Hassanzadegan et al, 2012).

The complete form of a quasi-static poroelastic deformation is given by Eq.2. It includes the strength of poroelastic coupling, i.e. the product of the Biot coefficient α and the Skempton coefficient B (Zimmerman, 2000):

$$\varepsilon_b = \frac{(1 - \alpha B)}{K_d} P - B \frac{(m - m_0)}{\rho_0 V_b^0} \quad (2)$$

where ε_b is the bulk strain of the porous rock, m is the change in fluid mass content per reference bulk volume V_b^0 , K_d is the drained bulk modulus, P is confining pressure, P_p is pore pressure, and ρ_0 is fluid density at reference conditions. The classical sign convention of rock mechanics is applied here: compressive stresses are considered to be positive.

The Biot coefficient α can be determined by considering the stress-strain behavior of the rock and performing jacketed and unjacketed experiments (indirect method):

$$\alpha = 1 - \frac{K_d}{K_s} \quad (3)$$

where K_s is the solid grain bulk modulus. The Skempton coefficient B can be calculated, knowing the static elastic moduli of the constituents and the bulk skeleton:

$$B = \left[1 + \phi^i \left(\frac{1}{K_d} - \frac{1}{K_s} \right)^{-1} \left(\frac{1}{K_f} - \frac{1}{K_s} \right) \right]^{-1} \quad (4)$$

where ϕ^i is the initial porosity at saturated conditions and K_f is the bulk modulus of the pore fluid.

Biot (1956a) employed the poroelastic equations as constitutive equations, in concert with the second law of Newton, and developed the theory of elastic wave propagation (dynamic theory of poroelasticity). The theory predicts the existence of three types of waves at high frequencies, compressional waves (P-waves, V_P) of first and second kinds and shear waves (S-waves, V_S). Two crucial parameters can be identified in this theory: a characteristic frequency ω_c , and an

acoustic velocity ratio η . The Biot characteristic frequency ω_c , which determines the transition from the low to the high frequency range, depends on the rock porosity ϕ and permeability k , as well as the fluid density ρ_f and viscosity μ_f ,

$$\omega_c = \frac{\phi\mu_f}{2\pi\rho_fk} \quad (5)$$

The acoustic velocity ratio $\eta = V_P/V_S$, i.e. the ratio between compressional and shear wave velocities, is the key parameter in determining dynamic elastic moduli (Castagna et al, 1985). The velocity ratio, $\eta = \frac{V_P}{V_S}$, is independent of bulk density and reflects the variations in Poisson's ratio, ν , of an isotropic solid,

$$\eta^2 = \left(\frac{V_P}{V_S}\right)^2 = \frac{2(1-\nu)}{1-2\nu} \quad (6)$$

Accordingly, the dynamic Poisson ratio reads,

$$\nu = \frac{\eta^2 - 2}{2\eta^2 - 2} \quad (7)$$

and the dynamic bulk modulus depends on the bulk density ρ_b and can be expressed as:

$$K = \rho_b V_S^2 [\eta^2 - 4/3] \quad (8)$$

3 Correlation of static and dynamic elastic moduli: drained velocity ratio

For a correlation of the static and dynamic elastic moduli, first we introduce the drained and undrained Poisson ratios, ν_d and ν_u , and then the corresponding velocity ratios. The principal assumption here is that ultrasonic wave velocities (of this special type of rock) are of an undrained nature, i.e. no change in fluid mass content is expected due to ultrasonic wave propagation (see section 6.3 in the support of this hypothesis). The drained and undrained Poisson ratios are related to shear modulus μ , K_d and K_u according to Detournay and Cheng (1993),

$$\nu_d = \frac{3K_d - 2\mu}{2(3K_d + \mu)} \quad (9a)$$

$$\nu_u = \frac{3K_u - 2\mu}{2(3K_u + \mu)} \quad (9b)$$

The magnitude of poroelastic effects is controlled by the strength of poroelastic coupling αB which can be written in terms of the drained and undrained Poisson ratios ν_d and ν_u (Detournay and Cheng, 1993):

$$\alpha B = 1 - \frac{K_d}{K_u} = \frac{3(\nu_u - \nu_d)}{(1 - 2\nu_d)(1 + \nu_u)} \quad (10)$$

Then, we adopt the strength of poroelastic coupling in terms of an drained velocity ratio, and an undrained velocity ratio as the fundamental set of governing equations.

Therefore, an undrained velocity ratio η_u can be determined by direct measurement of the ultrasonic wave velocities V_P and V_S where the dynamic elastic moduli are of undrained nature. A drained velocity ratio $\eta_d = \left(\frac{V_P}{V_S}\right)_d$ can be defined as the acoustic velocity ratio of a saturated porous rock when all the pores are connected and the induced pore pressure has time to equilibrate within the representative elementary volume (REV) by drainage of pore fluid. Knowing that $E = 2\mu(1 + \nu) = 3K(1 - 2\nu)$ (Mavko et al, 2003) and using Eq.6, the difference between the velocity ratios at drained and undrained conditions can be written as:

$$\begin{aligned} \left(\frac{V_P}{V_S}\right)_u^2 - \left(\frac{V_P}{V_S}\right)_d^2 &= \frac{2(1 - \nu_u)}{(1 - 2\nu_u)} - \frac{2(1 - \nu_d)}{(1 - 2\nu_d)} \\ &= \frac{K_u}{\mu} \frac{3(\nu_u - \nu_d)}{(1 - 2\nu_d)(1 + \nu_u)} \end{aligned} \quad (11)$$

It is assumed that the drained and undrained shear moduli are equal ($\mu = \mu_d = \mu_u$) as in Gassmann theory (Berryman, 1999). Replacing Eq.10 into Eq.11 yields:

$$\left(\frac{V_P}{V_S}\right)_u^2 - \left(\frac{V_P}{V_S}\right)_d^2 = \frac{K_u}{\mu} \alpha B \quad (12)$$

where K_u is undrained bulk modulus. Consequently, the drained acoustic velocity ratio η_d can be defined as:

$$\eta_d = \sqrt{\eta_u^2 - \frac{K_u}{\mu} \alpha B} \quad (13)$$

The derived drained velocity ratio, η_d , serves as input in Eq.8 to calculate the dynamic drained bulk modulus. The proposed correlation approach was validated by performing drained jacketed andunjacketed experiments on a Malm carbonate rock sample as described in the following.

4 Experimental procedures

4.1 Sample materials

The rock samples used in this study were collected from outcrops in the Molasse Basin, southwestern Germany. The Molasse basin is a foreland basin north of the Alps that formed due to continental collision.

As a target geothermal reservoir formation, the Upper Jurassic Malm underlies the Molasse sediments and is confined by the Mesozoic crystalline basement

Table 1: Mineral composition of Malm carbonate. Minerals were identified by XRD analysis. Bulk moduli of the minerals are taken from Mavko et al (2003) and the bulk modulus of titanium dioxid is taken from Carmichael (1984).

Mineral	chemical formula	mass fraction (%)	bulk modulus (GPa)
Calcium carbonate	CaCO_3	98.62	76.8
Magnesium carbonate	MgCO_3	0.44	161.4
Silica	SiO	0.04	37
Aluminium oxide	Al_2O_3	0.03	172
Iron oxide	Fe_2O_3	0.09	154
Potassium oxide	K_2O	0.23	-
Sodium oxide	Na_2O	0.12	-
Titanium dioxide	TiO_2	0.01	209.1

below and Cretaceous sandstone above. A 500 m thick Malm formation crops out in the Swabian Alps and the Franconian Mountains to the north of the river Danube. The Malm is well known for its lateral and vertical lithological heterogeneity. Three major lithofacies types can be distinguished with respect to fluid flow: *i*) massive or reef facies, *ii*) bedded facies, and *iii*) Helvetic facies (Hofmann et al, 2014). The massive facies is mainly dolomitized and has a high permeability, due to recrystallization and karstification. The bedded facies is composed of limestone, marly limestones, and minor dolomites and has a relatively low permeability. Finally, the Helvetic facies of deep marine environment has a very low permeability.

Outcrop analogue samples from the Malm δ (bedded limestone with sponges), Malm ϵ (massive limestone), and Malm $\zeta 6$ (bedded limestone) were collected and analyzed. A Malm $\zeta 6$ sample was selected for the investigations performed in this study. This rock contains mainly calcium carbonate (Table 1). A cylindrical sample with a diameter of 50 mm and 100 mm length was tested. The core sample has a porosity of 10.9%. The initial porosity was calculated by measuring dry weight, W_d , saturated weight in air, W_s , and the suspended (Archimedes) weight in water, W_a to be $\phi^i = (W_s - W_d)/(W_s - W_d)$.

4.2 Experimental setup and methods

The tests were performed in a conventional triaxial testing system (MTS 815). A complete description of the setup is given by Hassanzadegan et al (2012). A circumferential extensometer and two axial extensometers were mounted on the sample. Two types of piezo-ceramic transducers (P and S-type) generated the compressional wave signal V_P and the shear wave signal V_S at central frequencies close to 500 KHz. The P- and S-wave piezo-ceramic transducers were located on the top and bottom endcaps. The P and S-wave excitations were recorded by P- and S-type receivers, respectively. Data was visualized and recorded using an oscilloscope and stored and analyzed with Geopsy software, an open source

software for seismic analysis (Wathele, 2004). The net arrival times through the sample were determined by correcting for delay times. Two thermocouples were placed inside the pressure vessel to measure temperature. The temperature was increased using heating bands outside the pressure vessel. The pore pressure was controlled independently using Quizix pumps.

The experimental procedure started by preconditioning the sample to reduce inelastic effects during the subsequent poroelastic tests. First, the chamber temperature was increased to 60 °C and confining pressure was cycled, once between 0 MPa to 80 MPa at a rate of 0.6 MPa/min and then four times between 0 to 80 MPa at a rate of 2 MPa/min. Then, a vacuum pressure of 8 mbar was applied to the pore pressure system and the sample was fully saturated, first, by water imbibition at room temperature. That is, the upstream valve at the bottom of the sample was open to the water pump and the downstream valve was open to the vacuum pump. In order to ensure that saturation was complete the water was flowed for 120 hours at a pressure difference of 5 MPa between the upstream and downstream side of the sample, i.e. the upstream pressure was set at 14 MPa and the downstream one at 9 MPa. Moreover, the flow rate was recorded and after fluid flow stabilized the permeability of the sample was calculated using Darcy's law.

Then, preconditioning procedure was repeated and confining pressure was cycled four times between 0 to 80 MPa at a rate of 2 MPa/min. Two different types of poroelastic experiments were performed at two temperature levels (30 and 60 °C), one drained and one unjacketed experiment. During the drained experiment, the pore fluid pressure was kept constant at 2 MPa and the confining pressure was cycled between 3 and 80 MPa, resulting in an effective pressure of up to 78 MPa. Each cycle was composed of an upward ramp, a three hours plateau, and a downward ramp. A cycling rate of 0.09 MPa/min, lower in comparison to the one used for preconditioning (2 MPa/min), was applied. The unjacketed experiment was performed by increasing confining pressure up to 80 MPa applying the same cycling rate as in the drained experiment.

5 Results

The static poroelastic moduli of the Malm carbonate were measured by performing drained (jacketed) and unjacketed experiments. The Biot and Skempton coefficients were determined, and subsequently, the strength of poroelastic coupling, i.e. the product of Biot and Skempton coefficients, was calculated. The strength of poroelastic coupling served to define the drained velocity ratio and dynamic elastic moduli, respectively. The results are presented as a function of Terzaghi effective pressure, P' , i.e. the difference between confining pressure and pore pressure ($P - P_p$). The permeability of the tested Malm carbonate sample, as determined during preconditioning, was $0.69 \times 10^{-18} \text{ m}^2$ at an applied confining pressure of 25 MPa.

5.1 Static moduli and strength of poroelastic coupling

The loading-unloading stress-strain curves evidence a nonlinear behavior of the sample under drained conditions (Fig.1). Both curves indicate a hysteresis and some degree of irreversible behavior.

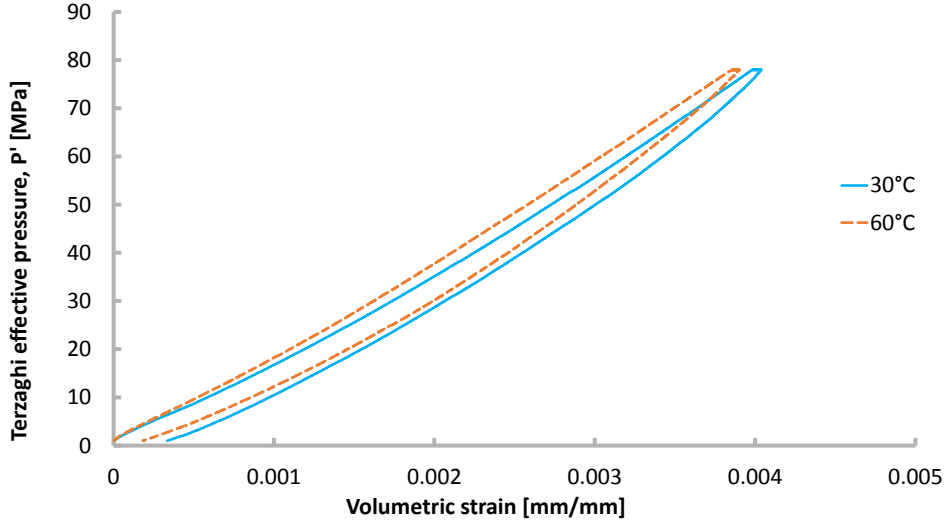


Figure 1: Effective pressure as a function of volumetric strain. The stress-strain curves display hysteresis, some degree of irreversibility, and non-linearity at drained conditions.

Figure 2 presents the unloading drained bulk moduli as the tangent slope of the stress-strain curves, $K_d = \frac{\partial P'}{\partial \varepsilon_b}$, at both 30 and 60 °C. The drained bulk modulus of the sample increased with increasing effective pressure at 30 and 60 °C. The strain measurement accuracy meets the requirements for calibration stipulated by the ISO 9513 class 0.5, i.e. 0.5% of reading or 1 μm of the indicated value, whichever is larger. The error involved in calculating the drained bulk modulus was estimated by partial derivatives of $K_d = \frac{\partial P'}{\partial \varepsilon_b}$ and the method of propagation of errors (see Eq.14) to range between 30 and 80 MPa at high and low effective pressures, respectively.

$$\left(\frac{\Delta K_d}{K_d}\right)^2 = \left(\frac{\Delta P'}{P'}\right)^2 + \left(\frac{\Delta \varepsilon_b}{\varepsilon_b}\right)^2 \quad (14)$$

Figure 3 shows the stress-strain curves at unjacketed conditions. The unjacketed bulk modulus, i.e. the average slope of the stress-strain curve, $K_s = \frac{\Delta P}{\Delta \varepsilon_b}$, increased with increasing temperature from 103.9 GPa at 30 °C to 112.2 GPa at 60 °C.

Figure 4 illustrates the Biot coefficient (Eq.3) as a function of Terzaghi effective pressure. The Biot coefficient at 60 °C is slightly higher than 30 °C. The

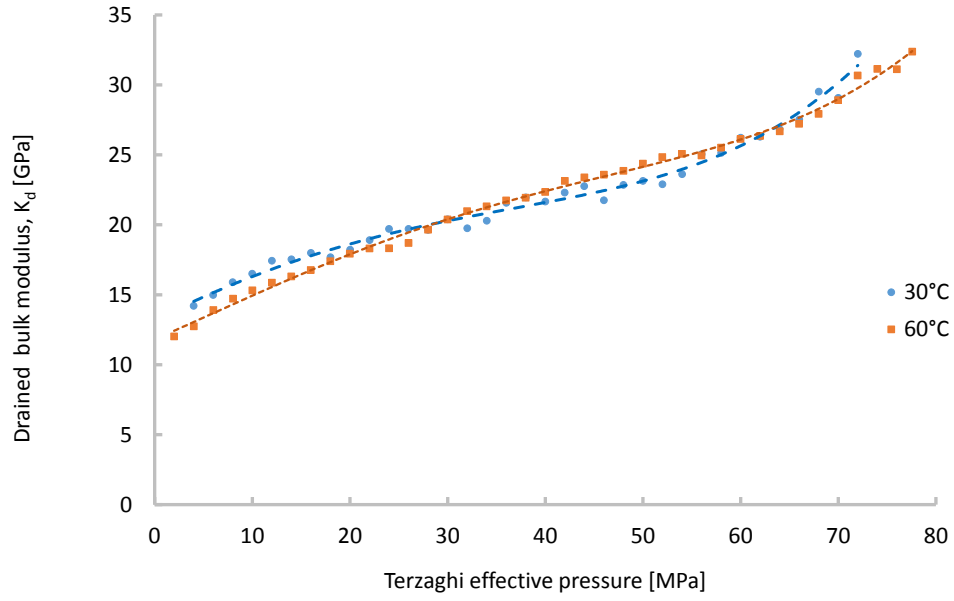


Figure 2: Drained bulk moduli at 30 and 60 °C as a function of Terzaghi effective pressure.

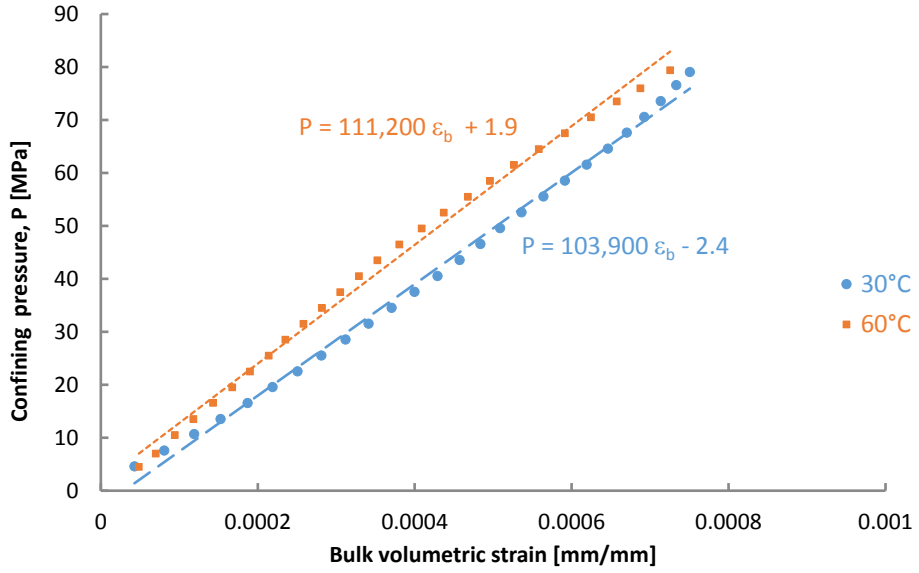


Figure 3: Confining pressure as a function of bulk volumetric strain at unjacketed conditions.

Biot coefficient decreases with increasing effective pressure. It ranges between 0.86 and 0.68 at 30 °C.

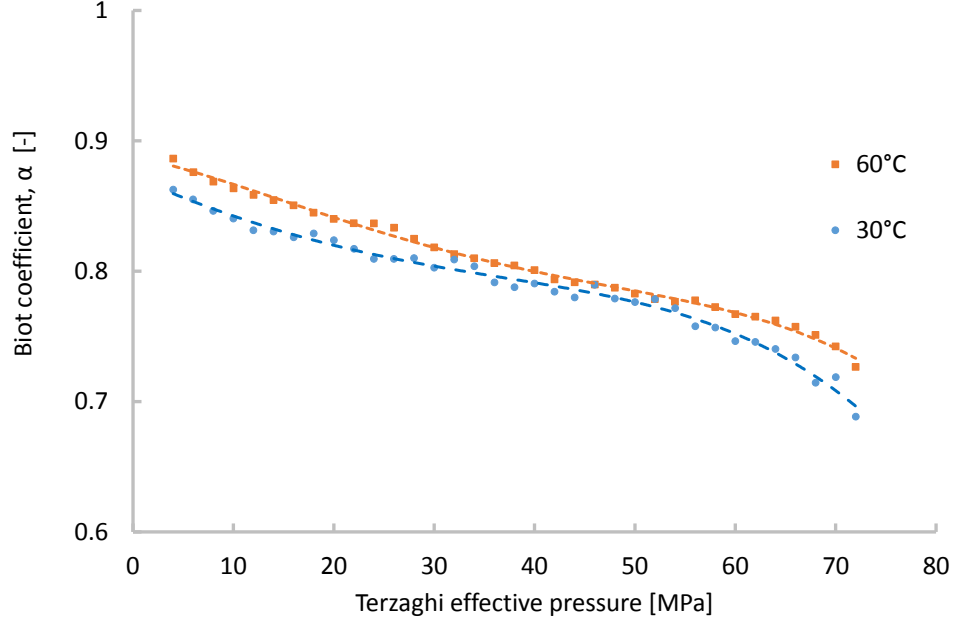


Figure 4: Biot coefficients as a function of Terzaghi effective pressure (Eq.3).

The Skempton coefficients at 30 and 60 °C were calculated using Eq.4 and are plotted in Fig.5. As effective pressure increases, the Skempton coefficient decreases. The Skempton coefficient at low pressures and 60 °C is slightly higher than 30 °C ones.

The strength of poroelastic coupling was calculated using Eq.2 from the product of Biot and Skempton coefficients (Fig.6). The strength of coupling decreases with increasing effective pressure. That is, the pore pressure response to a change in volumetric strain is weaker at higher effective pressures and is stronger at lower effective pressures. This parameter decreases with increasing effective pressure by about 56% from 0.51 at 3 MPa to 0.22 at 73 MPa.

5.2 Acoustic velocities and dynamic elastic moduli

The acoustic velocities were measured at pressure intervals of 5 MPa while performing the drained test. The arrival times for compressional and shear waves were picked using the Geopsy software and were confirmed by employing the Akaike Information Criterion, AIC (Akaike, 1974) (see Appendix B). The accuracy of arrival times was examined by plotting all the wavelets together and by tracking the onset times. As an example, a compressional wavelet, a shear wavelet, the picking time window, and the location of the onset times are shown

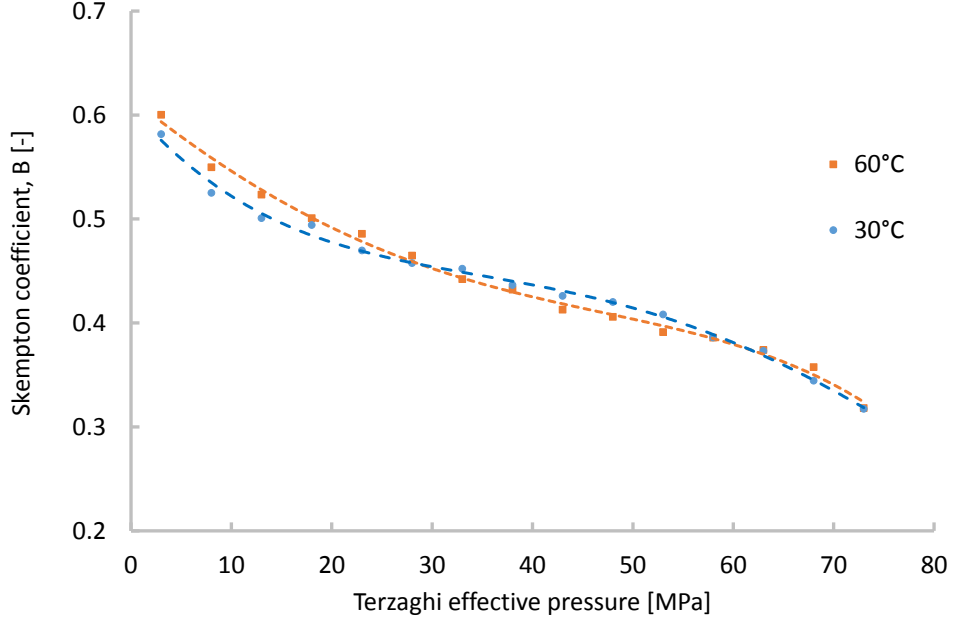


Figure 5: Skempton coefficients as a function of Terzaghi effective pressure (Eq.4).

in Fig.7.

Figures 8 and 9 present the compressional and shear wave velocities as a function of effective pressure at 30 and 60 °C, respectively. The P- and S-wave velocities approached a maximum value of about 5.12 and 2.68 *km/s* with increasing pressure at 30 °C, respectively. The P-wave velocity increased with increasing pressure by about 2.5% (from 4.99 to 5.12 *km/s*) and S-wave velocity increased by about 2.8% (from 2.60 to 2.68 *km/s*). At 60 °C, the P-wave velocity increased by about 3.0% (from 4.8 to 4.94 *km/s*) and S-wave velocity increased by about 2.73% (from 2.60 to 2.67 *km/s*).

The velocity ratios for 30 and 60 °C are presented in Fig.10. The difference between the velocity ratios at 30 and 60 °C is higher at low effective pressures and decreases towards high effective pressures, such that both curves converge. The average velocity ratios at 30 and 60 °C are 1.91 and 1.90, respectively.

The dynamic undrained Poisson ratio was calculated using Eq.8 (Fig.11). Poisson's ratio at 30 °C is higher than at 60 °C in average. The uncertainty in calculated Poisson's ratio can be estimated, using Eq.7 and the method of propagation of errors as follows,

$$\frac{\Delta\nu}{\nu} = f(\eta) \left[\left(\frac{\Delta V_P}{V_P} \right)^2 + \left(\frac{\Delta V_S}{V_S} \right)^2 \right]^{0.5} \quad (15)$$

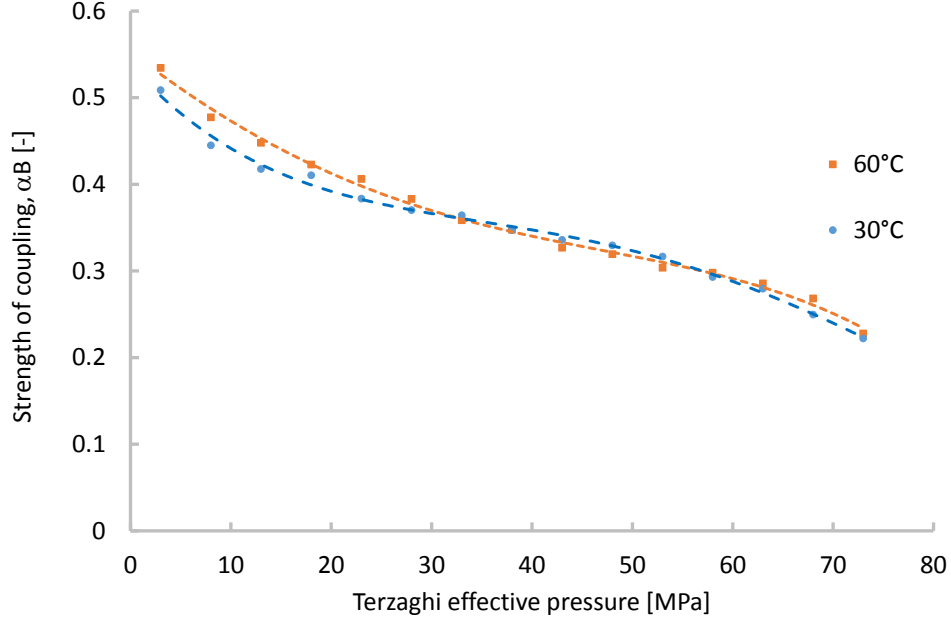


Figure 6: Strength of poroelastic coupling, αB , as a function of effective pressure.

where

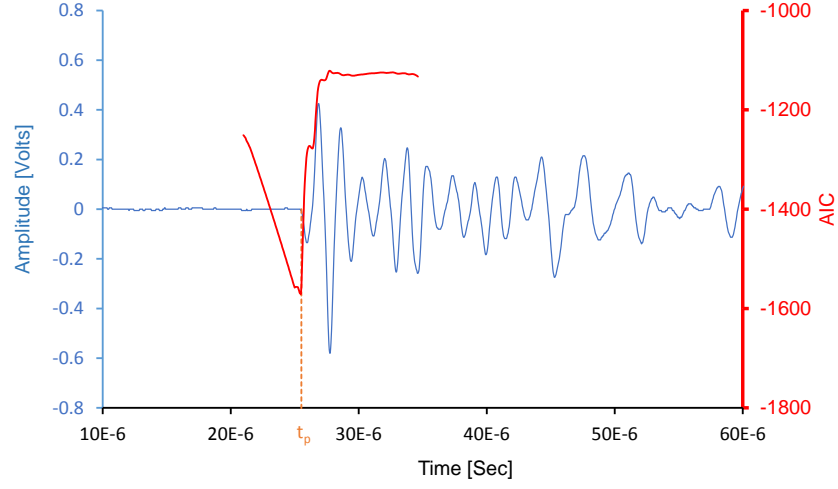
$$f(\eta) = \frac{2\eta^2}{(\eta^2 - 1)(\eta^2 - 2)} \quad (16)$$

A 0.1% error in laboratory measurements of V_P and V_S yields an error of 0.25% in Poisson's ratio (0.310 ± 0.001), whereas a maximum error of 2% in field measurements of V_P and V_S results in a 5% error in Poisson's ratio calculation (0.31 ± 0.015). At 30 °C, Poisson's ratio first decreases with increasing effective pressure and then increases after 60 MPa. At 60 °C, Poisson's ratio is almost constant at low to moderate effective pressures and increases with increasing effective pressure after 55 MPa.

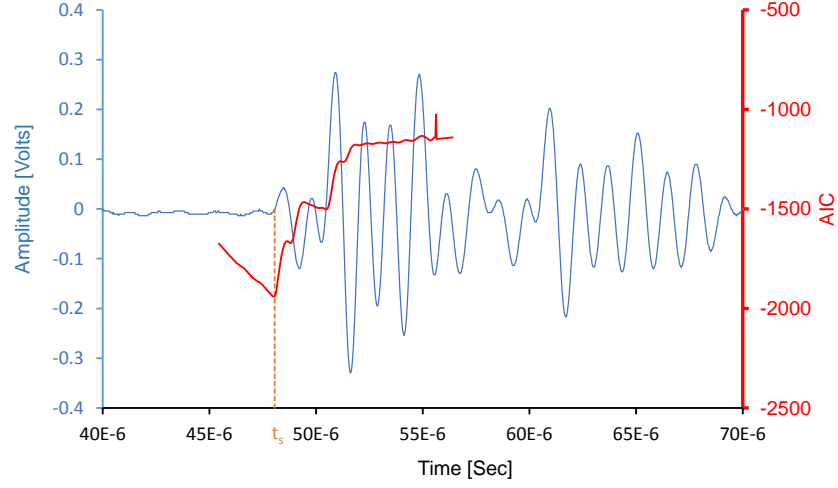
5.3 Relating static and dynamic elastic moduli

The undrained dynamic elastic bulk moduli were calculated, having obtained the ultrasonic velocity ratios and using Eq.8. The drained velocity ratio was determined by calculating the static poroelastic coupling parameter and the measured (undrained) velocity ratio (see Fig.12). The rate of change in drained velocity ratio with effective pressure at 60 °C is slightly higher than at 30 °C.

The value of $\frac{K_u}{\mu}$ in Eq.12 was obtained as best fit parameter. At 30 °C, it was equal to 3.26, corresponding to an undrained static Poisson's ratio of 0.28 (Eq.9b), and at 60 °C it was equal to 2.9, corresponding to an undrained static



(a) P-wavelet



(b) S-wavelet

Figure 7: Detecting the onset of arrival times (t_p and t_s) was performed by employing the Akaike Information Criterion (AIC) for both P- and S-wavelets. The minimum value of the AIC function corresponds to the first motion of the waves.

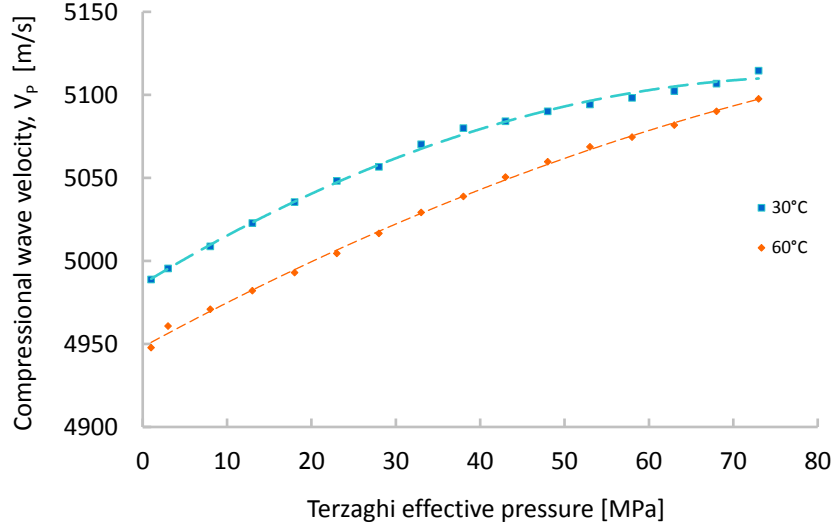


Figure 8: Compressional wave velocity V_P as a function of Terzaghi effective pressure at 30 and 60 °C.

Poisson’s ratio of 0.24. The drained bulk moduli were derived by employing Eq.8 and by substituting the drained velocity ratios that matched properly the measured static drained bulk moduli (Figs. 13 and 14).

6 Discussion

Previous studies tried to correlate the static and dynamic moduli either by correcting for stress-strain measurements, e.g. Fjaer (1999) and Holt et al (2012) or by defining compressional and shear wave velocities in terms of effective moduli and randomly distributed inclusions (Le Ravalec and Guéguen, 1996). Messop (2012) ascribed the difference between static and dynamic moduli to the time scale of pressure diffusion processes and the applied boundary conditions in a poroelastic medium. An effect of applied boundary conditions in quasi-static theory of poroelasticity is reflected here in drained and undrained velocity ratios that are related to drained and undrained Poisson ratios, respectively. The introduced correlation approach focuses on the velocity ratio which can be directly determined in seismological and geophysical studies (Audet et al, 2009). Albeit, there are some inherited assumptions and limitations.

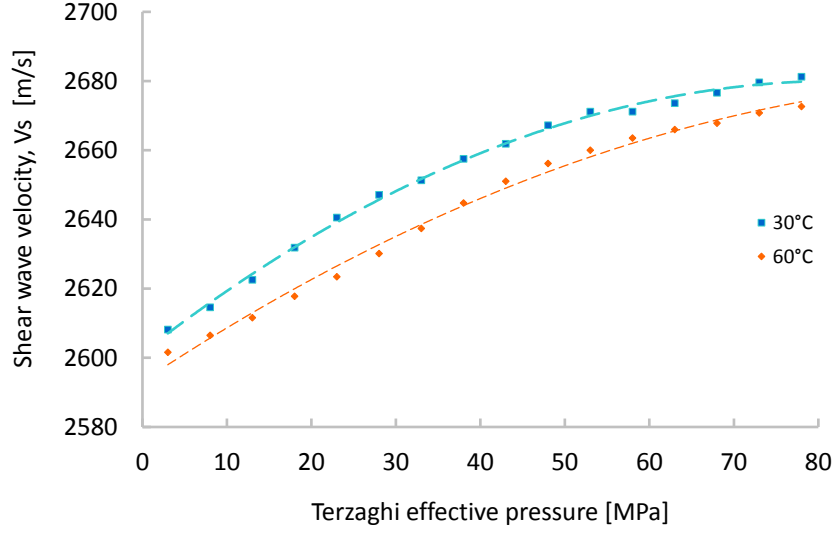


Figure 9: Shear wave velocity V_S as a function of Terzaghi effective pressure at 30 and 60 °C.

6.1 Assumptions and limitations

The correlation equation (Eq.12) derived from quasi-static Biot theory of poroelasticity and Gassmann's equation applies under the following conditions: *a)* the porous material is assumed to be linear, isotropic and elastic, *b)* the porous rock is completely saturated, *c)* the bulk density is assumed to be constant, *d)* the porous rock consists of one type of pores such that all pores have the same stiffness, *e)* the shear moduli at drained and undrained conditions are equal, *f)* all pores are well connected and the pore pressure is equilibrated within REV *g)* the induced pore pressures are equilibrated through the pore space at low and moderate frequencies, and *h)* the velocity dispersion and attenuation, as a result of scattering, viscoelastic and solid dissipation, etc. are negligible.

It was assumed that the porous medium is isotropic and Poisson's ratio is directly related to the velocity ratio. In this case, the velocity ratio generally trends between the velocity ratio of the mineral grains and the values for a suspended mixture of fluid and minerals. However, in an anisotropic medium the Poisson ratio and the velocity ratio depend on the orientation of wave propagation, crack density, and crack geometry (Walsh, 1966; Mavko et al, 2003).

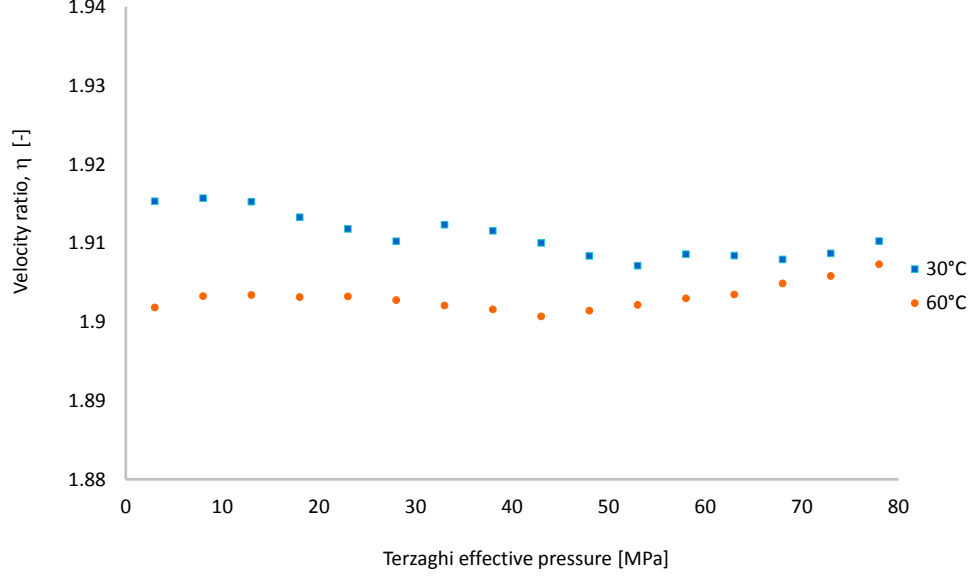


Figure 10: Velocity ratio η as a function of Terzaghi effective pressure at 30 and 60 °C.

6.2 Elastic wave propagation theories

The fundamental equations of elastic wave propagation were derived by assuming that dissipation only depends on the relative motion between the fluid and the solid (Biot, 1956b). Several other dissipation mechanisms can be assumed, such as viscoelastic and solid dissipation (Biot, 1962), and different wave propagation theories can be derived for porous and cracked media as reviewed by Le Ravalec and Guéguen (1996) and Sarout (2012). Each characteristic (cut-off) frequency is related to a dissipation mechanism and categorizes the wave propagation theories into different domains. In addition, each characteristic frequency determines the transition from a low to a high frequency range, corresponding to relaxed and unrelaxed dynamic moduli, respectively (Le Ravalec and Guéguen, 1996; Mavko et al, 2003) which should be distinguished from drained and undrained moduli.

6.3 Drained and undrained conditions in low frequency range

In this experimental study, static and dynamic moduli were simultaneously measured. Therefore, two different types of deformations may occur concurrently; a macroscopic deformation due to applied hydrostatic confining pressure, and a microscopic deformation due to passage of an ultrasonic stress wave that may

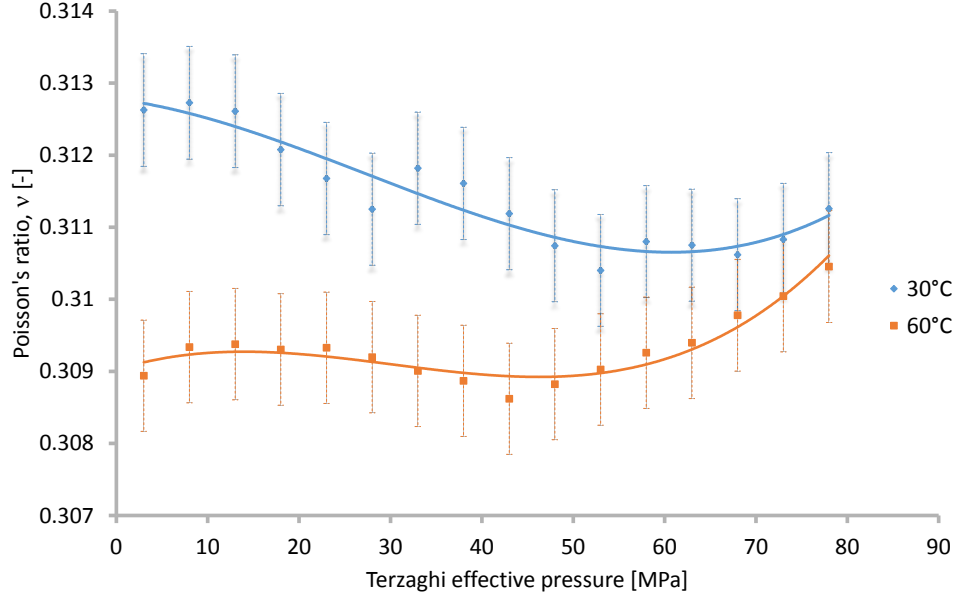


Figure 11: Poisson's ratio ν as a function of Terzaghi effective pressure at 30 and 60 °C.

induce pore pressure gradients on the scale of individual pores.

In quasi-static theory of poroelasticity, the drained and undrained moduli refer to deformation of the REV and reflect the type of hydraulic boundary conditions applied to an idealized continuous medium, i.e. the static moduli are macroscopic effective moduli defined over an REV. The drained and undrained dynamic moduli are characterized by time dependent processes (e.g., the pore pressure diffusion and crack closure) within an REV and by hydraulic and mechanical boundary conditions. Therefore, not only heterogeneities and spatial distribution of the microscopic properties (e.g., crack aspect ratio and pore radius) are of importance but also the diffusivity coefficient of the rock under consideration as well as the applied loading rate play an important role (Detournay and Cheng, 1993; Le Ravalec and Guéguen, 1996). That is, how fast the induced pore pressure due to the applied stress wave equilibrated with pressures at the boundaries.

The Biot characteristic frequency separates the quasi-static and dynamic domains of poroelasticity theory, corresponding to a low and a high frequency range, respectively (Le Ravalec and Guéguen, 1996; Sarout, 2012). The Biot characteristic frequency of the tested Malm carbonate was calculated using Eq.5 to be 13.2 GHz ($k=0.69 \times 10^{-18}$, $\mu_f = 8 \times 10^{-4}$ and $\phi=0.109$). The ultrasonic frequency in the laboratory (500 KHz) was always less than the Biot characteristic frequency. Therefore, the ultrasonic velocity measurements and derived

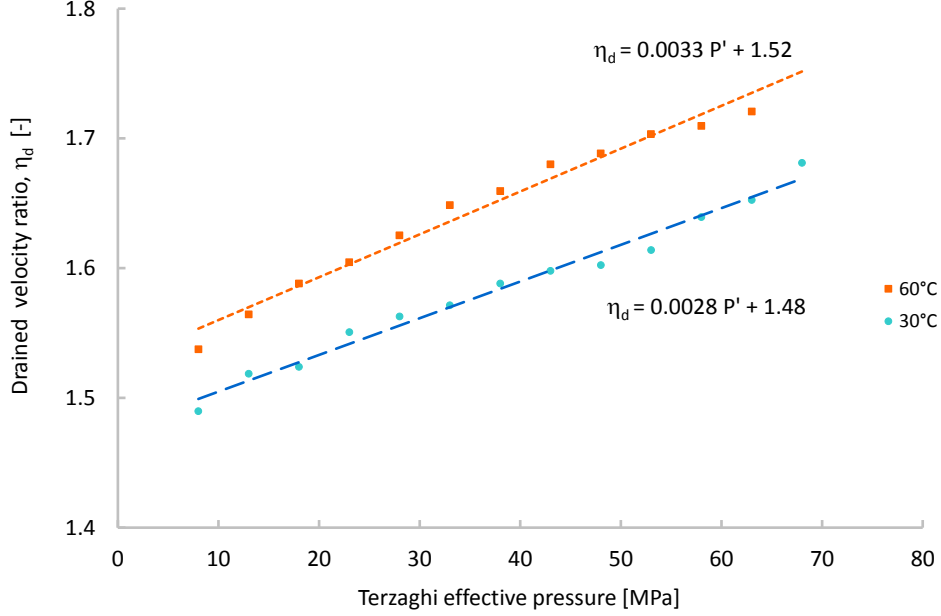


Figure 12: Drained velocity ratio η_d as a function of Terzaghi effective pressure at 30 and 60 °C (see Section 3).

dynamic elastic moduli remain in low-frequency range in the framework of dynamic poroelasticity. Consequently, the Gassmann's equation is applicable.

The tested Malm carbonate sample was drained at both ends. The characteristic time for pore pressure diffusion is of the order of $L^2/4D$, where D is the diffusivity coefficient and L is the length of the core (see Appendix C). The diffusivity coefficient determines characteristic time of the diffusion and is proportional to the permeability of the rock. The permeability of the Malm carbonate was calculated to be $0.69 \times 10^{-18} \text{ m}^2$ at an applied confining pressure of 25 MPa (an average effective pressure of 12.5 MPa). The measured permeability value is in agreement with those reported by Homuth et al (2015) for Malm carbonate at high effective pressures. At low effective pressures Homuth et al (2015) reported a total shift of about 2-3 order of magnitudes in the permeability of the Malm carbonate. The pressure dependence of the permeability of a limestone rock sample was investigated by (Ghabezloo et al, 2009). It was concluded that a pore pressure decrease or an increase in confining pressure both result in a decrease of the permeability, albeit the effect of pore pressure is more pronounced.

Having measured permeability of the tested Malm sample, the diffusivity coefficient was calculated to be of the order of magnitude of $1 \times 10^{-4} \text{ m}^2/\text{s}$ (see Appendix C, Eq.C.1). Therefore, the time required for the pore pressure to reach equilibrium as a result of a sudden load is about 60 s. The time scale

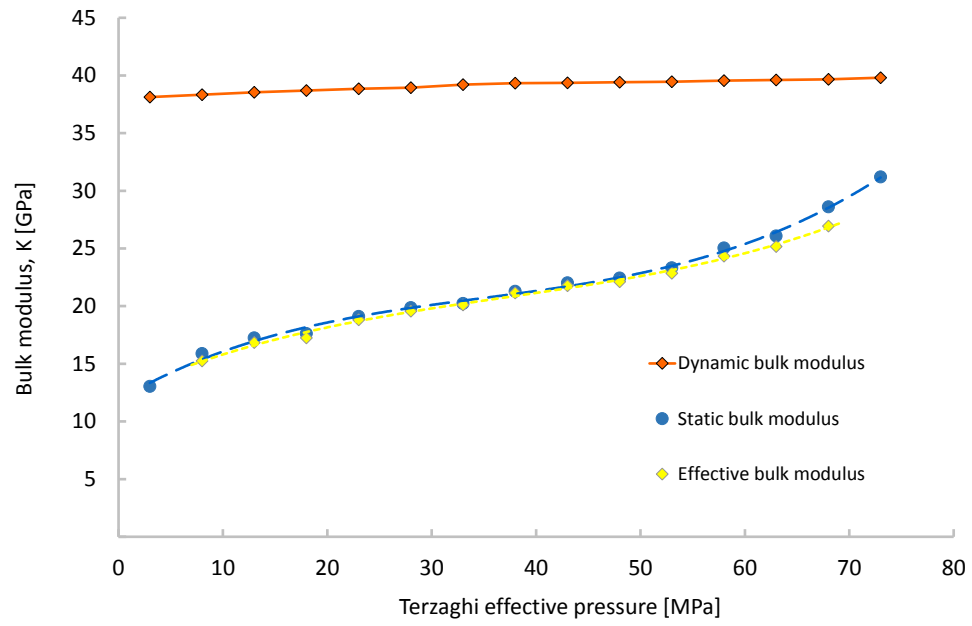


Figure 13: Bulk moduli as a function of Terzaghi effective pressure at 30 °C. The effective drained bulk modulus was calculated by substituting the drained velocity ratio in Eq.8. The calculated effective and measured static bulk moduli matched well.

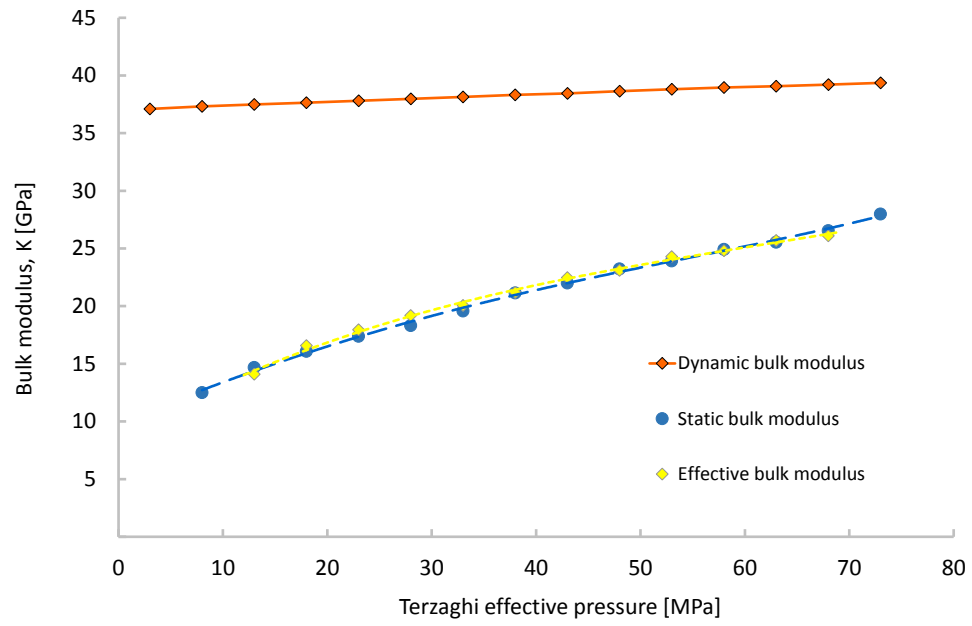


Figure 14: Bulk moduli as a function of Terzaghi effective pressure at 60 °C. The effective drained bulk modulus was calculated by substituting the drained velocity ratio in the Eq.8. The calculated effective and measured static bulk moduli matched well.

of stress wave propagation is inversely proportional to the frequency and is equal to 2×10^{-6} s. The time scales of pore pressure diffusion and the stress wave propagation differ by seven orders of the magnitude such that microscopic deformations can be assumed to be undrained ones. Therefore, the ultrasonic wave propagation, the velocity ratios, and the related dynamic elastic moduli are of undrained nature. Moreover, the applied confining pressure rate 0.09 MPa/min is low enough (in comparison to a sudden load, i.e. an infinite rate) such that pore pressure has enough time to be equilibrated with pressures at the boundaries.

6.4 Poroelastic and dynamic moduli of Malm carbonate

The static and dynamic moduli of the tested Malm carbonate increased with increasing effective pressure and the same behavior has been observed for other types of rock, e.g. sandstone (Fjaer, 1999) and chalk (Alam et al, 2012). The stress-strain curves showed hysteresis and irreversibility while loading and unloading the sample. This indicates that part of the work done on the sample is dissipated. Part of the strains were not recovered immediately after unloading (see Fig.1) which can be assigned to time dependent deformation of the sample (e.g., creep, anelasticity, plasticity, etc.). The principal assumption behind this analysis is that stress cycling effects has been minimized after applying preconditioning procedure (see section 4.2).

The value of theunjacketed bulk modulus 103.9 GPa (see Fig.3) was observed to be higher than those reported for calcite (76.8 GPa) and dolomite (94.9 GPa) minerals (Mavko et al, 2003). Such high values for theunjacketed bulk modulus have been reported previously for a limestone of the same age (da Silva et al, 2010). The value of theunjacketed bulk modulus of this late Jurassic rock varied between 60 and 210 GPa at 25.5 MPa effective pressure. If the mineral composition is assumed to be homogeneous, a constantunjacketed bulk modulus equal to the mineral bulk modulus is expected. However, if isolated pores and isolated micro-cracks are present, as expected for carbonate rock, theunjacketed bulk modulus may differ from the mineral bulk modulus and approaches a higher value. Moreover, the composition of the tested Malm carbonate shows existence of different oxides with bulk moduli higher than 150 GPa (see Table 1) that influences theunjacketed stiffness of the porous rock.

Dimensionless poroelastic coefficients, such as the Biot coefficient, the Skempton coefficient and the strength of poroelastic coupling, decreased with increasing effective pressure (see Figs. 4, 5 and 6). That is, the degree of coupling between deformation and pore pressure decreases with increasing effective pressure and pore pressure less effectively counteracts the applied confining pressure resulting in lateral deformation of grains into the pore space and to altering porosity. Porosity variations and changes in micro-structure provide a link between poroelastic and dynamic moduli. Since values of pore stiffness K_ϕ are rather difficult to be directly measured, the common assumption is that $K_\phi = K_s$ (Hart and Wang, 1995). In the current study, an indirect method (Eq. 3) was used to calculate the Biot coefficient using the static elastic moduli. An alternative

approach for determining the poroelastic coupling parameter is to measure the Biot and Skempton coefficients directly, without measuring static elastic moduli. That is, the fluid mass content can be monitored to obtain Biot’s coefficient, and the Skempton coefficient can be measured as the ratio of the induced pore pressure to the change in applied confining pressure for undrained conditions (Hassanzadegan et al, 2012; Blöcher et al, 2014). This has the advantages that no stress-strain measurements are required and the effective velocity ratio can be related directly to the poroelastic coupling parameter.

The poroelastic coupling parameter served to accommodate for the nonlinearity of the dynamic bulk modulus and to include the changes in Poisson’s ratio. At low effective pressures, the value of the poroelastic coupling parameter is high, low aspect ratio pores are open, and Poisson’s ratio is less than its intrinsic value, i.e. Poisson’s ratio of the rock without cracks (Walsh, 1965). At high effective pressures, the value of the poroelastic coupling parameter decreases, low aspect ratio pores are closed, and Poisson’s ratio increases with increasing effective pressure (Walsh, 1965). That is, at high pressures not only the low aspect ratio pores are closed but also the grains deform into the pore space due to Poisson’s effect, i.e. compression at grain contacts causes the grains to become shorter in the direction of the compressive load and wider laterally thereby lowering the effective porosity of the rock. Consequently, acoustic velocity increases.

The acoustic velocities were in the range of those reported for Cobourge limestone (Nasseri et al, 2013) and were increasing with increasing effective pressure (see Figs.8 and 9). Both V_P and V_S decreased with increasing temperature from 30 to 60 °C. While heat treatment, the thermally induced microcracks, and increasing crack porosity may lower the acoustic velocities, which has also been observed for Bourgogne limestone (Lion et al, 2005) and Flechtinger sandstone (Hassanzadegan et al, 2013).

Since the ultrasonic acoustic velocity ratios are of undrained nature, the derived Poisson ratios are also of undrained nature. It appears that this correlation (Eq.12) provides the correct nonlinear link between drained and undrained velocity ratios via the strength of poroelastic coupling parameter αB .

Two terms are associated with any discussion of error analysis: accuracy and precision. While the accuracy is a measure of the closeness to the true value, the precision refers to reproducibility of the measurements. The error calculations presented here refer to the accuracy of the results rather than their precision. Thus, this study becomes a starting point for further investigations at in-situ conditions, for a wide range of frequencies and confining pressures, and including different rock types.

6.5 Implications

6.5.1 Earthquakes and induced seismicity

At the time of an earthquake the static stress change can be considered negligible (Brennguier et al, 2014). However, when seismic energy is released, part of the

energy propagates through the crust as seismic body waves resulting in dynamic stress changes, i.e. as transient stress perturbations (Brenguier et al, 2014). Due to the short time scale of an earthquake in comparison to the rate of fluid flow, undrained conditions are favored in the fluid saturated zones and a higher velocity ratio in comparison to drained conditions is expected. There are some observations and evidence that confirm this hypothesis. For example, passive-source seismic imaging suggested the existence of a zone of high velocity and Poisson ratios down-dip of a subduction ridge which was attributed to high pore fluid pressures and low effective pressures (Brenguier et al, 2014). Moreover, Segall (1989) has shown that poroelastic contraction of a zone from which fluid are produced can destabilize faults and induce seismicity in areas where the fluid mass content does not change (i.e. in undrained zones).

Providing the suggested correlation, it would be possible to characterize undrained zones in terms of poroelastic moduli by comparing seismic images before and after induced seismicity or earthquakes.

6.5.2 Mechanical reservoir characterization and monitoring

The presented correlation not only can be used for geomechanical reservoir characterization but also it is important for underground reservoir management and the recognition of the overpressured and underpressured zones within geothermal and hydrocarbon reservoirs before and after exploitation. First, the poroelastic moduli in concert with acoustic velocities of a rock sample, representative for the target formation, have to be measured in the laboratory. Then, the derived correlation between acoustic velocity ratios and the poroelastic moduli serves to characterize the reservoir formation, having obtained the field measurements of acoustic velocities. In other words, by comparing initial and modified velocity ratios, the in situ effective pressure and the corresponding poroelastic moduli can be derived.

7 Conclusions

In this study static drained bulk moduli of Malm carbonate were correlated to the dynamic elastic bulk moduli. A novel correlation approach was presented based on Biot theory of poroelasticity and wave propagation. The strength of poroelastic coupling parameter, i.e. the product of Biot and Skempton coefficients, was the central element of this coupling approach. A drained velocity ratio was introduced and was linked to the drained Poisson ratio. The Biot and Skempton coefficients, as well as their products, i.e. the strength of poroelastic coupling, were pressure dependent and were decreasing with increasing pressure. The value of the strength of poroelastic coupling parameter decreased with increasing effective pressure by about 56% from 0.51 at 3 MPa to 0.22 at 73 MPa. In contrast, the P- and S-wave velocities changed by a maximum of 3% in this pressure range. The P- and S-wave velocities approach a maximum value of about 5.12 and 2.68 km/s, respectively, with increasing pressure at 30

°C. The average velocity ratios at 30 and 60 °C were 1.91 and 1.90, receptively. The calculated drained bulk moduli using the effective velocity ratios matched the measured static drained bulk moduli well.

The proposed correlation approach not only is important in detecting and characterizing low and high effective pressure zones within subduction zones but also is important in underground reservoir management for recognizing and characterizing overpressured and underpressured zones within geothermal and hydrocarbon reservoirs, e.g., by comparing velocity ratios before and after injection or production.

8 Acknowledgments

The authors would like to thank Liane Liebeskind for assistance with the laboratory experiments and TU Bergakademie Freiberg for providing XRD data. Furthermore, the authors would like to thank the reviewers for their constructive comments. This work has been performed in the framework of the Allgäu geothermal project and was funded by the Federal Ministry for the Environment, Nature Conservation, Building and Nuclear Safety, Germany (Grant 0325267B).

Nomenclature

Latin Letters

a	fitting parameter	
B	Skempton coefficient	$[-]$
b	fitting parameter	
E	Young's modulus	Pa
K_d	drained bulk modulus	Pa
K_ϕ	pore stiffness	Pa
K_u	undrained bulk modulus	Pa
K_f	pore fluid bulk modulus	Pa
K_s	solid grain bulk modulus	Pa
K_u^{dy}	dynamic undrained bulk modulus	Pa
m	fluid mass content	kg
m_0	reference fluid mass content	kg
P	confining pressure	Pa
P'	Terzaghi effective pressure	Pa
P_p	pore pressure	Pa
$\frac{V_p}{V_s}$	velocity ratio	$[-]$
V_b^0	reference bulk volume	m^3
V_P	compressional wave velocity	m/s
V_S	shear wave velocity	m/s
W_a	suspended weight of the sample	kg
W_d	dry weight of the sample	kg

W_s	saturated weight of the sample	kg
-------	--------------------------------	------

Greek Letters

α	Biot coefficient	$[-]$
αB	strength of poroelastic coupling	$[-]$
ρ_b	bulk density	kg/m^3
η	velocity ratio	$[-]$
η_d	drained velocity ratio	$[-]$
η_u	undrained velocity ratio	$[-]$
ε_b	bulk strain	$[-]$
ν	Poisson's ratio	$[-]$
ν_d	drained Poisson's ratio	$[-]$
ϕ	porosity	$[-]$
ϕ^i	initial porosity	$[-]$
ρ_0	reference fluid density	kg/m^3
σ_{kk}	first stress invariant	Pa
μ	shear modulus	Pa
μ_d	drained shear modulus	Pa
μ_u	undrained shear modulus	Pa

9 Appendices

A Gassmann equation

Gassmann's equation relates the drained to the undrained bulk moduli. Gassmann's equations can be written in terms of the strength of the poroelastic coupling αB (Berryman, 1999):

$$K_u = \frac{K_d}{1 - \alpha B} \quad (A.1)$$

$$\mu_d = \mu_u \quad (A.2)$$

This relation (Eq.A.1) shows how the stiffness of a loaded rock is related to the strength of the poroelastic coupling. In principle, the drained and undrained shear moduli, i.e. μ_d and μ_u , are identical (Berryman, 1999). At low frequencies, the Gassmann equation relates the drained and undrained elastic moduli (Le Ravalec and Guéguen, 1996).

B Picking the arrival-times of ultrasonic waves

A review of time-picking techniques is given by Sarout et al (2009). The Akaike Information Criterion (AIC) was used for picking arrival-times of ultrasonic waves. The AIC picker is a statistical function for which the global minimum

defines the onset time of the signal as described by Akaike (1974), Akazawa (2004) and Kurz et al (2005).

$$AIC(J) = J \cdot \log(\text{var}(R(1, J))) + (N - J - 1) \cdot \log(\text{var}(R(1 + J, N))) \quad (\text{B.1})$$

This formulation applies two sliding ranges (windows) to the signal, where J is a counter range through the signal and N is the total number of data samples. \log and var denote the logarithm and variance functions and $R(a, b)$ determines the interval range of the recorded voltage.

C Transient poroelasticity

The coupling of fluid mass diffusion with volumetric deformation results in a coupled pore pressure diffusion, i.e. the pore pressure diffusion is coupled with the rate of change of the volumetric strain. The diffusivity coefficient D can be written in terms of drained and undrained elastic moduli, the mobility ratio $\frac{k}{\mu_f}$, and poroelastic coefficients to be (Guéguen and Boutéca, 2004),

$$D = \frac{BK_u}{\alpha} \frac{k}{\mu_f} \frac{(K + \frac{4\mu}{3})}{(K_u + \frac{4\mu}{3})} \quad (\text{C.1})$$

References

- Akaike H (1974) Markovian representation of stochastic processes and its application to the analysis of autoregressive moving average processes. *Annals of the Institute of Statistical Mathematics* 26(1):363–387
- Akazawa T (2004) A technique for automatic detection of onset time of p and s-phases in strong motion records, 13th World conference on earthquake engineering vancouver, b.c., canada. In: 13th World Conference on Earthquake Engineering, pp 1–9
- Alam MM, Fabricius IL, Christensen HF (2012) Static and dynamic effective stress coefficient of chalk. *Geophysics* 77(2):L1–LL11
- Audet P, Bostock MG, Christensen NI, Peacock SM (2009) Seismic evidence for overpressured subducted oceanic crust and megathrust fault sealing. *Nature* 457:76–78
- Berryman JG (1999) Origin of Gassmann’s equations. *Geophysics* 64(5):1627–1629
- Biot MA (1941) General theory of three-dimensional consolidation. *Journal of Applied Physics* 12(2):155–164
- Biot MA (1956a) Theory of propagation of elastic waves in a fluid-saturated porous solid. i. low-frequency range. *Journal of the Acoustical Society of America* 28(2):168–178

- Biot MA (1956b) Theory of Propagation of Elastic Waves in a Fluid-Saturated Porous Solid. II. higher-Frequency Range. *The Journal of the Acoustical Society of America* 28:179–191
- Biot MA (1962) Generalized theory of acoustic propagation in porous dissipative media. *The Journal of the Acoustical Society of America* 34(9A):1254–1264
- Blöcher G, Reinsch T, Hassanzadegan A, Milsch H, Zimmermann G (2014) Direct and indirect laboratory measurements of poroelastic properties of two consolidated sandstones. *International Journal of Rock Mechanics and Mining Sciences* 67:191 – 201
- Brenguier F, Campillo M, Takeda T, Aoki Y, Shapiro NM, Briand X, Emoto K, Miyake H (2014) Mapping pressurized volcanic fluids from induced crustal seismic velocity drops. *Science* 345(6192):80–82
- Cacace M, Blöcher G, Watanabe N, Moeck I, Börsing N, Magdalena-Scheck-Wenderoth, Kolditz O, Huenges E (2013) Modelling of fractured carbonate reservoirs: outline of a novel technique via a case study from the molasse basin, southern bavaria, germany. *Environmental Earth Sciences* 70(8):3585–3602
- Carmichael R (1984) Handbook of physical properties of rocks, *Handbook of Physical Properties of Rocks*, vol v. 3. Taylor and Francis
- Carroll M (1980) Mechanical response of fluid saturated porous materials. In: *Theoretical and Applied Mechanics*, Proc. 15th Int. Congress of Theoretical and Applied Mechanics, Toronto, August 1723, F. P. J. Rimrott and B. Tabarrok, eds., North-Holland, Amsterdam, pp 251–262
- Castagna JP, Batzle ML, Eastwood RL (1985) Relationships between compressional-wave and shear-wave velocities in clastic silicate rocks. *Geophysics* 50(4):571–581
- Detournay E, Cheng AHD (1993) Fundamentals of poroelasticity. In *Comprehensive Rock Engineering: Principles, Practice and Projects*, vol 2, Pergamon Press, chap 5, pp 113 –169
- Eissa E, Kazi A (1988) Relation between static and dynamic young’s moduli of rocks. *International Journal of Rock Mechanics and Mining Sciences and Geomechanics Abstracts* 25(6):479 – 482
- Fjaer E (1999) Static and dynamic moduli of weak sandstones. In: *Rock Mechanics for Industry* Amadei, B., Kranz, RL, Scott, GA, Smeallie, Balkema, pp 675–681
- Gassmann (1951) Über die Elastizität poröser Medien. *Vierteljahrsschrift der Naturforschenden Gesellschaft* 96:1–23

- Ghabezloo S, Sulem J, Gudon S, Martineau F (2009) Effective stress law for the permeability of a limestone. *International Journal of Rock Mechanics and Mining Sciences* 46(2):297 – 306
- Guéguen Y, Boutéca M (2004) *Mechanics of Fluid Saturated Rocks*. Elsevier Academic Press
- Hart DJ, Wang HF (1995) Laboratory measurements of a complete set of poroelastic moduli for berea sandstone and indiana limestone. *Journal of Geophysical Research: Solid Earth* 100(B9):17,741–17,751
- Hassanzadegan A, Blöcher G, Zimmermann G, Milsch H (2012) Thermoporoelastic properties of flechtinger sandstone. *International Journal of Rock Mechanics and Mining Sciences* 49(0):94 –104
- Hassanzadegan A, Blöcher G, Milsch H, Urpi L, Zimmermann G (2013) The effects of temperature and pressure on the porosity evolution of Flechtinger sandstone. *Rock Mechanics and Rock Engineering* 47(2):421–434
- Heerden W (1987) General relations between static and dynamic moduli of rocks. *International Journal of Rock Mechanics and Mining Sciences and Geomechanics Abstracts* 24(6):381 – 385
- Hofmann H, Blöcher G, Börsing N, Maronde N, Pastrik N, Zimmermann G (2014) Potential for enhanced geothermal systems in low permeability limestones: stimulation strategies for the western Malm karst (Bavaria). *Geothermics* 51:351 – 367
- Holt RM, Nes OM, F SJ, Fjaer E (2012) Static vs. dynamic behavior of shale. In: *American Rock Mechanics Association, 46th U.S. Rock Mechanics/Geomechanics Symposium*, 24-27 June, Chicago, IL, USA
- Homuth S, Götz AE, Sass I (2015) Reservoir characterization of the upper jurassic geothermal target formations (molasse basin, germany): role of thermofacies as exploration tool. *Geothermal Energy Science* 3(1):41–49, DOI 10.5194/gtes-3-41-2015
- King MS (1969) Static and dynamic elastic moduli of rocks under pressure. In: *The 11th U.S. Symposium on Rock Mechanics (USRMS)*, June 16 - 19, 1969, Berkeley, CA, pp 329–351
- Kurz JH, Grosse CU, Reinhardt HW (2005) Strategies for reliable automatic onset time picking of acoustic emissions and of ultrasound signals in concrete. *Ultrasonics* 43(7):538 – 546
- Le Ravalec M, Guéguen Y (1996) High- and low-frequency elastic moduli for a saturated porous/cracked rock-differential self-consistent and poroelastic theories. *Geophysics* 61(4):1080–1094

- Lion M, Skoczylas F, Ledésert B (2005) Effects of heating on the hydraulic and poroelastic properties of bourgogne limestone. *International Journal of Rock Mechanics and Mining Sciences* 42(4):508–520
- Mavko G, Mukerji T, Dvorkin J (2003) *The Rock Physics Handbook: Tools for Seismic Analysis of Porous Media*. Cambridge University Press
- Messop A (2012) When to use static or dynamic moduli in geomechanical models. In: 46th US Rock Mechanics / Geomechanics Symposium , 24-27 June, held in Chicago, IL, USA
- Nasseri M, Goodfellow S, Wanne T, Young R (2013) Thermo-hydro-mechanical properties of cobourg limestone. *International Journal of Rock Mechanics and Sciences, Mining* 61:212–222
- Nur A, Byerlee JD (1971) An effective stress law for elastic deformation of rock with fluids. *Journal of Geophysical Research* 76:6414–6419
- Sarout J (2012) Impact of pore space topology on permeability, cut-off frequencies and validity of wave propagation theories. *Geophysical Journal International* 189(1):481–492
- Sarout J, Ferjani M, Guguen Y (2009) A semi-automatic processing technique for elastic-wave laboratory data. *Ultrasonics* 49(45):452 – 458
- Sayers CM, Schutjens PMTM (2007) An introduction to reservoir geomechanics. *The Leading Edge* 26(5):597–601
- Segall P (1989) Earthquakes triggered by fluid extraction. *Geology* 17(10):942–946
- da Silva MR, Schroeder C, Verbrugge JC (2010) Poroelastic behaviour of a water-saturated limestone. *International Journal of Rock Mechanics and Mining Sciences* 47(5):797–807
- Simmons G, Brace WF (1965) Comparison of static and dynamic measurements of compressibility of rocks. *Journal Of Geophysical Research* 70:5649–5656
- Walsh JB (1965) The effect of cracks in rocks on poisson’s ratio. *Journal of Geophysical Research* 70(20):5249–5257
- Walsh JB (1966) Seismic wave attenuation in rock due to friction. *Journal of Geophysical Research* 71(10):2591–2599
- Wang Z (2000) Dynamic versus static elastic properties of reservoir rocks. In: *Seismic and Acoustic Velocities in Reservoir Rocks: Recent developments, Seismic and Acoustic Velocities in Reservoir Rocks*, Society of Exploration Geophysicists, pp 531–539
- Wathele M (2004) Geopsy project. In: Grenoble, France, URL <http://www.geopsy.org>

- Yale DP, Jamieson WH (1994) Static and dynamic mechanical properties of carbonates. In: Rock Mechanics, Balkema, Rotterdam
- Zimmerman R (2000) Coupling in poroelasticity and thermoelasticity. International Journal of Rock Mechanics and Mining Sciences 37(1-2):79 – 87